

## PLUTO AND CHARON WITH THE *HUBBLE SPACE TELESCOPE*. II. RESOLVING CHANGES ON PLUTO'S SURFACE AND A MAP FOR CHARON

MARC W. BUIE<sup>1</sup>, WILLIAM M. GRUNDY<sup>2</sup>, ELIOT F. YOUNG<sup>1</sup>, LESLIE A. YOUNG<sup>1</sup>, AND S. ALAN STERN<sup>1</sup>

<sup>1</sup> SwRI, 1050 Walnut Street, Suite 300, Boulder, CO 80302, USA; [buie@boulder.swri.edu](mailto:buie@boulder.swri.edu), [efy@boulder.swri.edu](mailto:efy@boulder.swri.edu),  
[layoung@boulder.swri.edu](mailto:layoung@boulder.swri.edu), [alan@boulder.swri.edu](mailto:alan@boulder.swri.edu)

<sup>2</sup> Lowell Observatory, 1400 West Mars Hill Road, Flagstaff, AZ 86001, USA; [grundy@lowell.edu](mailto:grundy@lowell.edu)

Received 2009 May 29; accepted 2009 November 18; published 2010 February 4

### ABSTRACT

We present new imaging of the surface of Pluto and Charon obtained during 2002–2003 with the *Hubble Space Telescope* (*HST*) Advanced Camera for Surveys (ACS) instrument. Using these data, we construct two-color albedo maps for the surfaces of both Pluto and Charon. Similar mapping techniques are used to re-process *HST*/Faint Object Camera (FOC) images taken in 1994. The FOC data provide information in the ultraviolet and blue wavelengths that show a marked trend of UV-bright material toward the sunlit pole. The ACS data are taken at two optical wavelengths and show widespread albedo and color variegation on the surface of Pluto and hint at a latitudinal albedo trend on Charon. The ACS data also provide evidence for a decreasing albedo for Pluto at blue (435 nm) wavelengths, while the green (555 nm) data are consistent with a static surface over the one-year period of data collection. We use the two maps to synthesize a true visual color map of Pluto's surface and investigate trends in color. The mid- to high-latitude region on the sunlit pole is, on average, more neutral in color and generally higher albedo than the rest of the surface. Brighter surfaces also tend to be more neutral in color and show minimal color variations. The darker regions show considerable color diversity arguing that there must be a range of compositional units in the dark regions. Color variations are weak when sorted by longitude. These data are also used to constrain astrometric corrections that enable more accurate orbit fitting, both for the heliocentric orbit of the barycenter and the orbit of Pluto and Charon about their barycenter.

**Key words:** astrometry – planets and satellites: individual (Charon, Pluto) – planets and satellites: surfaces

**Online-only material:** color figures, supplementary data files, digital image files

### 1. INTRODUCTION

Unresolved hemispherically averaged, rotationally resolved measurements of the Pluto–Charon system form the foundation of our current understanding of this distant world. Despite the wealth of information gleaned from such work there remain questions that can only be answered by higher spatial resolution observations (cf., Stern 1992). Until the arrival of the New Horizons spacecraft (Young et al. 2008), our most effective tool appears to be the *Hubble Space Telescope* (*HST*). With its ultra-stable point-spread function (PSF) and quality of calibration it can provide photometrically accurate information with a few resolution elements across the disk of Pluto. Some ground-based observatories have been able to reach similar spatial resolution in the near-infrared, typically at *H* and *K* bands, but these data lack the extensive observational record available at visible wavelengths. The optical data, typically at *B* and *V* bands, are only sensitive to continuum reflectance and as a result are simpler to interpret. The near-IR data are further complicated by including spectral regions that include both continuum and strong methane absorptions. Having good maps over time in the optical are a critical first step needed to support interpretations of other data sets.

Pluto is approximately 2300 km in diameter and the best maps deliver information at spatial scales of a few hundred kilometers at best. This situation means that our present investigations are completely inadequate for establishing the geologic context of the surface. However, this scale is sufficient to place important constraints on volatile transport. The surface albedo pattern and its time evolution must be quantified before we can develop credible models that can be used to interpret unresolved

photometry and spectroscopy and make predictions on the nature of the surface and atmosphere interaction and its evolution through a full Plutonian year.

Owing to our limited angular resolution capabilities, even the seemingly unrelated task of describing the orbit of Charon is affected by the albedo variations on the surface of Pluto. The contrast and scale of these variations lead to a non-negligible shift of the photocenter of Pluto that is synchronous with the orbit. If this variation is not properly removed from the astrometric signal the derived orbit will be in error. The long-standing question of the eccentricity of Charon's orbit is another issue that is limited by our knowledge of the map of Pluto yet has important implications for the dynamical history of the system.

All of these issues become even more important for the process of planning the New Horizons encounter with Pluto in 2015. We need to be able to do simple things like predict exposure times. We also need to predict where the objects will be at the time of encounter. The fast flyby speed requires that we select one hemisphere of Pluto for the most detailed set of observations and mapping helps guide our guesses on the most interesting portions of the surface.

This paper is the second of a two-part series and presents disk-resolved albedo observations of Pluto and Charon. The first paper (Paper I) covered the disk-integrated nature of the newest epoch of *HST* data. Our new work builds on the heritage of past efforts that began with the earliest spot models (Marcialis 1988; Buie & Tholen 1989), continued with mutual event mapping (Buie et al. 1992), and moved on to the first epoch of *HST* mapping (Stern et al. 1997). Here, we report on a re-analysis of the 1994 Faint Object Camera (FOC) data that provides

improved photometrically accurate maps that supersede those published by Stern et al. (1997). A second epoch of *HST*-based imaging is also presented for the first time. These new data were taken in 2002–2003 with the High-resolution Camera of the Advanced Camera for Surveys (ACS/HRC). In this work, we present maps at two different optical wavelengths (equivalent to *B* and *V*) and attempt a true-color representation of Pluto's surface. We also include an investigation into the astrometric consequences of these results. Finally, we provide discussions on the time evolution of the surface that is complementary to the results from Paper I.

## 2. OBSERVATIONS

### 2.1. FOC Data

As reported in an earlier paper (Stern et al. 1997, hereafter SBT), our objective was to obtain the highest-possible resolution on Pluto that *HST* can achieve. We used the FOC in its highest resolution mode and collected images at blue and ultraviolet wavelengths where the diffraction resolution limit is most favorable. The FOC data were taken during an *HST* observing run in mid-1994, in which we obtained eight UV-bandpass (F278M, aka. UV) FOC images and 12 visible-bandpass (F410W, aka. VIS) FOC images of Pluto. The data were collected in 1994 within a single rotation of Pluto at 90° longitude spacing and a mean sub-Earth latitude of +12°7.

We estimated that 4–5 resolution elements could be placed across Pluto's diameter, and therefore, that a global Mercator projection map with  $\approx 40$ –55 independent resolution elements could be achieved. This resolution offers the opportunity to resolve the major albedo provinces on the planet, and discriminate between the various indirect-mapping solutions obtained from light curve and mutual event photometry. Additionally, by obtaining images on either side of the well-established,  $\sim 3000$ –3700 Å absorption edge of refractory materials which acts as a discriminator between contaminated and pure ice regions (e.g., Wagner et al. 1987), we were able to obtain information on the purity of the surface ices as a function of their location, a wholly new kind of input to volatile transport models.

As described in SBT, we reduced all 20 of these images, and identified the prominent surface reflectance features on them. Based on these images, we reported that Pluto's appearance is dominated by bright polar regions, and a darker but highly variegated equatorial zone which displays four bright subunits. The darkest unit on the equatorial zone appears to lie very close to the sub-Charon point and appears to be ringed by a bright fringe. The two poles of Pluto are both bright, but they are not identical: the northern polar region appears to be both larger and brighter. Each of Pluto's bright polar regions appears to display a ragged border.

In SBT, we also derived complete maps of Pluto in the VIS and UV filter bands in which the planet was imaged. These maps were generated by wrapping the images onto a rectilinear map grid and then stacking them all onto a single averaged stack. The resulting map has no photometric fidelity but is useful for noting the general location and morphology of surface features. Numerous artifacts are present in the map that are due to foreshortening toward the limb combined with limb darkening. A more complete description of those data is provided in SBT and is not repeated here. Our new map extraction methodology works on the exact same underlying imaging data as the earlier work but avoids the problems of the earlier mapping effort.

### 2.2. ACS/HRC Data

Our second epoch of observations is data taken with the ACS and its HRC. These data were obtained from 2002 June to 2003 June and are summarized in Paper I (a complete listing of all images and supporting information can be found in the supplemental files available in the online journal). Each visit was designed to occur at a specific sub-Earth longitude (Elon) on Pluto.<sup>3</sup> There were 12 visits in all, giving a 30° longitude spacing and a range of sub-Earth latitude of +28°3 to +32°3. These visits were scheduled throughout Cycle 11 so that the spacecraft roll angle would vary as much as possible over all visits while also covering a wide range of solar phase angles.

The ACS instrument does not have as fine a pixel scale as the FOC but this deficiency was made up for in other ways. Unlike the FOC, the camera has a high-quantum efficiency detector that does not suffer from count rate limits. As a result, ACS collected an image in less than a minute that was equivalent to a 20–30 minute integration with FOC. A sample of raw images is shown in Figure 1 in comparison with the earlier FOC images. The coarser pixel scale required substantial dithering to reach the full diffraction limit of the telescope but the fast cycle time of the instrument made this task possible. These characteristics of ACS/HRC also led to tremendously higher photometric signal-to-noise ratios compared to FOC and permitted collecting high-quality information on Charon as well as Pluto.

Each visit incorporated an identical sequence of observations and was designed to fit in a single *HST* visibility window. A key strategy to obtaining the full diffraction limited resolution results was a thorough dithering plan which consisted of a 16-exposure pattern listed in Table 1. The dithering pattern optimally fills a unit pixel cell with 16 unique fractional *X* and *Y* positions combined with a larger 80 pixel pattern to guard against localized problems with the detector. The visit was filled with one pattern of 12 s exposures with the F435W filter (Johnson *B* equivalent) followed by an identical pattern of 6 s exposures with the F555W filter (Johnson *V* equivalent). In all, we obtained 384 ACS images of the Pluto–Charon system with 192 images in each filter.

Most of the discussion regarding the processing of the raw images can be found in Paper I. However, two key steps warrant further discussion here. The pipeline images were individually measured to determine the sky background level which was then subtracted. The sky level was always very low and uniform across the array and contributed negligible noise to the data. The sky-subtracted data were further modified by multiplying by the pixel-area map to convert the data from surface brightness to detected photons per pixel.

Our data were collected with ACS/HRC in its first year of operation on *HST* and as a result are minimally affected by hot pixels and charge transfer problems. Our analysis was greatly enhanced by the high-quality calibration work that has been published on this instrument. We used the distortion maps and pixel-area maps of Anderson & King (2004). The PSF information we needed was provided by TinyTim version 6.2 (Krist 2004). The photometric calibration and transformation was provided by Sirianni et al. (2005).

<sup>3</sup> For this work, we use the same coordinate system for Pluto and Charon as in Buie et al. (1997) and Stern et al. (1997); that is, a right-handed coordinate system (hence east longitude), and the north pole is in the direction of the rotational angular momentum. 0° longitude passes through the sub-Pluto point on Charon and the sub-Charon point on Pluto at periaipse.

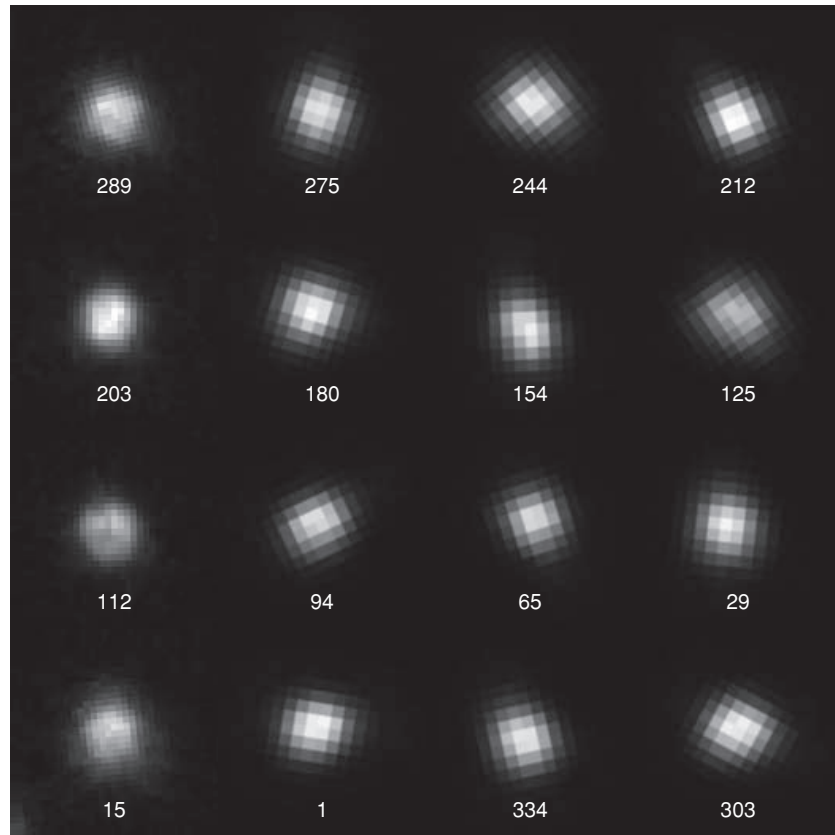


**Figure 1.** Sample raw images of Pluto. The numbers beneath each image are the sub-Earth East longitude (degrees) for that view. The leftmost column of images is the sample of FOC data shown in Stern et al. (1997). The other columns show a sample from the newer ACS/HRC data without removing the optical distortions inherent in the newer camera. The image scale is chosen such that Pluto is roughly the same size in all images. The coarser sampling is quite evident in the ACS data set. The images have all been rotated to put Pluto’s spin-north pole at the top. Pluto appears elongated in the ACS images in pseudo-random orientations as a result of the optical distortions and the large variation of spacecraft roll angle through the data collection. The images are scaled by brightness, within each camera’s data set, so that the light curve information is preserved.

### 3. FORWARD MODELING

#### 3.1. Fitting Concepts

Here we describe our approach to fitting all of the image data sets in a process we call forward modeling. This method starts with the requirement that data values (in this case image pixels) are never modified or manipulated beyond the needs of the calibration. As such, the images are a time-stamped grid providing a spatially resolved flux measurement collected over a field of view encompassing the Pluto system.

Our task in fitting the data is then reduced to a description of the scene that we think we are viewing. In this case, we have two objects that can be well approximated as spheres illuminated by the Sun that reflect light to our telescope and detector. Implicit in this approach is that we describe the sphere as having an albedo or other surface reflectance property that is allowed to vary as a function of location on the sphere. In our case, a map of the surface is actually a description of the single-scattering albedo which varies over the surface.

From this map, we can compute an image of Pluto and Charon at an arbitrarily high spatial resolution on the plane-of-the-sky given the geometric aspects for each image. We then downsample this perfect image, conserving flux, to an ideal image grid appropriate to the instrument, convolve with a PSF, and apply the geometric distortion factors (if needed). The resulting image is intended to reproduce what would be

observed by the instrument. This model image can then be iterated through its free parameters (i.e., map values) using nonlinear least-squares minimization to find the map that best fits the data. This process thus fits a single, static map to a given set of image data simultaneously and can take full advantage of any overlap and dithering between images to find an answer that best describes all images. In the interest of investigating time variability of the surface we chose to treat the FOC and ACS data sets as completely independent rather than solving for one map for all data.

#### 3.2. Model Parameters

Our forward model requires a priori knowledge of the geometry of the problem. For the radii of the objects we adopted a value of 1151 km for Pluto to be consistent with Buie et al. (1992) and 606 km for Charon (Sicardy et al. 2006, based on an early pre-publication value). The viewing geometry, latitude and longitude of the sub-solar and sub-Earth points, and position angle of the rotation axis, were computed with the same Charon ephemeris as used by Buie et al. (1992). While none of these values are considered to be the best, the errors thus introduced are small compared to the intrinsic errors of the mapping process. This work was spread over such a long duration and the size of the computation effort was so large that it precluded a last-minute update to these values. The last geometric variable was the position of the objects in the image, which was fitted for in each image.

**Table 1**  
Dither Pattern

Step	POSTARG	
	$x$ (arcsec)	$y$
1	0.000	0.000
2	-0.363	-0.421
3	-0.726	-0.842
4	-1.089	-1.263
5	0.200	0.116
6	-0.163	-0.305
7	-0.525	-0.726
8	-0.888	-1.147
9	0.085	0.316
10	-0.278	-0.105
11	-0.641	-0.526
12	-1.004	-0.947
13	-0.116	0.200
14	-0.479	-0.220
15	-0.842	-0.641
16	-1.205	-1.062

The model also clearly requires information about the PSF of the instrument. For the FOC data we used high-quality observed PSFs that matched the filters we used (the same PSFs as used by SBT). For the ACS/HRC data we used TinyTim to compute numerical PSFs that are based on the mean color of the object. Thanks to the work of Brown & Trujillo (2004) we knew to also fit for the telescope focus on each image. Based on this prior work, we had hoped to fit a focus trend with *HST* orbital longitude and thus reduce the number of free parameters in the model. Unfortunately, the sampling pattern and the actual focus trends of our data precluded such a simple approach. As a result, we were forced to fit the focus independently on all images.

We used the Hapke scattering theory (Hapke 1993) to compute the reflected light from the surface of Pluto (and Charon for the ACS data). Our approach in adapting the Hapke theory to this analysis follows very closely to the Buie et al. (1992) mutual event mapping. However, Buie et al. (1992) used the simplest form of the Hapke bidirectional reflectance equation from Hapke (1981), which makes no corrections for macroscopic surface roughness. We have now added this term to our calculation as well as incorporating the newer definition for  $h$ , the surface compaction parameter (Hapke 1984). We found the macroscopic roughness term to be critical in providing computationally sensible center-to-limb profiles. Without this term, points on the extreme edge of the disk take on unphysically high  $I/F$  values, high enough to add a non-trivial contribution to the integral over the disk in our calculations. Adding the roughness term, with almost any value for  $\bar{\theta}$ , eliminates this numerical difficulty and the reflectance at the limb behaves sensibly.

In all, there are five free parameters that must be specified for each map element so that a reflected flux can be computed. These parameters are  $w$ , single scattering albedo;  $h$ , surface compaction parameter;  $\overline{P(g)}$ , the single scattering particle phase function averaged over the small range of phase angle ( $g$ ) we sample;  $B_0$ , the backscatter correction factor; and  $\bar{\theta}$ , the average surface slope. It is a common practice to use a Henyey-Greenstein function (one or two parameters) for  $P(g)$  and then fit for the coefficients of the function. However, our phase angle range is so small and does a very poor job of constraining this function. Our approach, consistent with our past publications, is to use a constant value for our data. This value,  $\overline{P(g)}$ , does not make any assumptions about the functional form but simply gives a constraint on any future choice of  $P(g)$ .

**Table 2**  
Global Hapke Parameters

Set	$h$	$\overline{P(g)}$	$B_0$	$\bar{\theta}$	$\chi_{\text{VIS}}^2$	$\chi_{\text{UV}}^2$
A	0.1	2.5	0.8	10	1.26	0.76
B	0.07	2.5	0.53	10	1.27	0.76
C	0.05	2.5	0.39	10	1.28	0.76
D	0.11	2.0	1.0	10	1.27	0.76
E	0.122	3.0	1.0	10	1.25	0.78
F	0.1	2.5	0.8	30	1.27	0.76
Ch	0.0039	2.52	0.53	20	...	...

We do not have sufficient data to determine all these quantities for each surface element. As is commonly done, we use global values for all of these parameters except for the single scattering albedo. The choice for the global scattering parameters is not entirely arbitrary. As was done in Buie et al. (1992), we used the global photometric properties of Pluto to constrain these values. When we started this project the data did not yet yield a unique set of values, so we produced a number of plausible sets of parameters that spanned the plausible range of values expected on the surfaces of Pluto and Charon.

To constrain the global values, we used a sphere with a uniform single-scattering albedo of  $w = 0.8$ . We then compute the disk-integrated magnitude over the same range of solar phase angles possible for Pluto (and Charon) in 1992. By picking a value of  $h$ , we searched for the values of  $\overline{P(g)}$  and  $B_0$  that would match a phase coefficient of  $\beta = 0.0294 \text{ mag deg}^{-1}$  for Pluto and  $\beta = 0.0866 \text{ mag deg}^{-1}$  for Charon from Buie et al. (1997). We found the phase behavior to be completely insensitive to surface roughness, not surprising since surface roughness does not become truly important until the phase angle reaches  $30^\circ$ – $40^\circ$  (Hapke 1984). Therefore, we chose values for  $\bar{\theta}$  that seemed consistent with other similar surfaces in the solar system. The value chosen for  $\bar{\theta}$  for Pluto was based on Triton, though we tried one test using a larger value (set F). The Charon values were chosen to be consistent with other water-ice surfaces. The results of this calculation are summarized in Table 2. Sets A–F describe global values that all mimic the phase behavior of Pluto. The last set (Ch) is consistent with the phase behavior of Charon (see Paper I). Given the input constraints, none of these values were unique and a suite of parameters was chosen for Pluto to facilitate some consistency checks in fitting the FOC data. However, note that all of these parameter sets include a large value for  $\overline{P(g)}$ , indicating the particles have a backscattering lobe in their single-particle phase function.

Our fitting process works in absolute flux units ( $\text{erg cm}^{-2} \text{ s}^{-1}$ ). The images are converted from instrumental counts to flux by using the PHOTFLAM header value. The conversion from bidirectional reflectance to absolute flux uses the known geocentric and heliocentric distance of Pluto ( $\Delta$  and  $r$ , respectively) as well as the absolute flux of the Sun integrated over the instrumental bandpass. The steps required to go from the list of free parameters to something that is compared directly to the data are as follows:

1. The list of map value free and fixed parameters is converted from its lookup table to a small ( $18 \times 10$  for ACS data,  $20 \times 10$  for FOC data) regular grid. This grid of single-scattering albedo is expanded by pixel replication to a  $360 \times 200$  grid. The fitting grids with the converged values of  $w$  are shown in Figure 2 for Pluto and in Figure 3 for Charon. This expanded grid is then smoothed by a spherical

Gaussian filter with an FWHM of  $15^\circ$  ( $30^\circ$  for Charon) on the surface of the sphere. The choice of sub-sampling factors was made by requiring the photometric error from the rendered images as a function of sub-Earth longitude to be no worse than 0.1%. The width of the Gaussian filter was chosen to impose a limit on the spatial frequencies in the output image comparable to the diffraction limit of *HST*. The unconstrained polar regions were combined with cells that are visible near the winter terminator. By replicating the regions from the terminator to the invisible pole the calculation becomes numerically well behaved. The total number of free parameters in the FOC map grid was 144, while the ACS/HRC map has 114. The Charon ACS/HRC map grid has 25 free parameters.

2. A bidirectional reflectance image was computed from the smoothed map for the appropriate sub-Earth and sub-solar latitude and longitude at a scale that is a factor of 23 smaller than the undistorted pixel scale for HRC and a factor of 10 for FOC. The choice of the pixel scale was a compromise between speed of execution (lower is faster) and numerically well behaved (larger is better). This scale includes a conversion from the spatial scale in kilometers based on the radius of Pluto (or Charon) to arcseconds and all the geometric information (e.g.,  $r, \Delta$ ) unique to each exposure. The sub-sampling factor was chosen to keep the photometric errors of the finite rendered grid at or below 0.1%. This test was done by computing the numerical integral over the disk on the rendered image as a function of the position in the image plane. Numerical integration noise is seen as the position is moved across the scale of a single pixel and this quantity is minimized by the chosen sampling scale. The position at which this image is located introduces two free parameters in the rendered image calculation. The known orientation of the image, as described by the ORIENTAT keyword, was applied so that the position angle of Pluto's rotation axis in the rendered image matches that angle on the undistorted sky plane as seen in each image.
3. The sub-sampled sky-plane image is then binned down by pixel summation to match the instrumental pixel gridding scale. Finally, the computed image is then combined with the appropriate PSF including distortion if needed. At the end of this step, we have an image that can be directly compared to the data.

Our fitting process used the above steps to compute a weighted goodness-of-fit statistic for the given set of data and a unique set of free parameters. Not all free parameters are solved for at the same time. The fitting is broken into three discrete steps: (1) fit the map, (2) fit the positions, and (3) fit the focus (ACS data only). For each of the steps, the other free parameters are held constant. The order in which the steps are performed does not affect the final answer but the convergence time was reduced by alternately fitting the map, fitting the positions, re-fitting the map, fitting focus, re-fitting the map again, and so on until no changes were seen at any step.

### 3.3. FOC Model

The reference solar flux at 1 AU used by the FOC model was  $184 \text{ erg cm}^{-2} \text{ s}^{-1}$  for the F410W filter and  $22.6 \text{ erg cm}^{-2} \text{ s}^{-1}$  for the F278M filter and was derived by integrating over the instrumental response from the solar atlas of A'Hearn et al. (1983). Map fits were completed for all six sets of

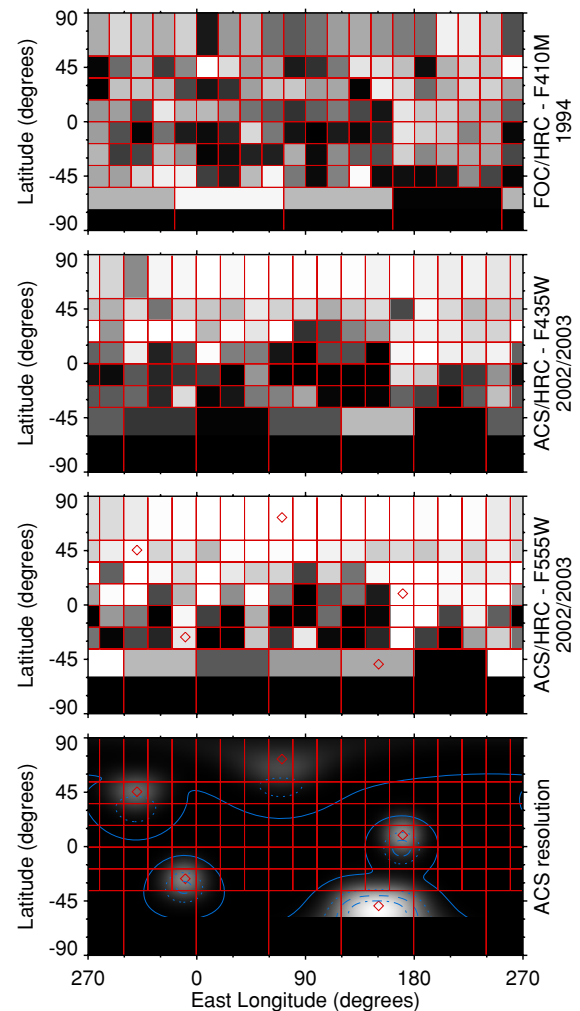


**Figure 2.** Free-parameter gridding for Pluto map solution. The surface of Pluto is broken up into a grid where each (gray or red) outlined zone is one free parameter of single-scattering albedo. The albedos shown are from the final fitted results. The grid for the FOC data (F410W 1994) is based on a  $20 \times 10$  array. The grid for the ACS data (F435W, F555W 2002/2003) is based on an  $18 \times 10$  array. Blocks of elements in the array are grouped together to more closely match the spatial resolution on the surface and the constraints possible from the data. The bottom segment of the plot shows the change in a map after the spherical smoothing for the ACS map caused by a change of 0.01 in select free parameters in the grid. The contours are shown at a change of 0.001 (solid), 0.02 (dotted), 0.04 (dashed), and 0.06 (dash-dotted) in single scattering albedo. The diamonds mark the location in the map where the change was inserted. This result gives an indication of the spatial resolution possible with this map reconstruction.

(A color version of this figure is available in the online journal. Supplemental digital source data and software is available online.)

Hapke scattering parameters. For this problem, an arbitrary interpolation of the Pluto model onto the FOC image grid was not considered feasible. The supporting calculations only permitted specifying the position to the nearest 0.1 pixel. Fitting for the map, position, and sky background level was done separately. While fitting one, the other two elements were held constant and the process of fitting each in turn was continued until reaching a final stable result that no longer changed. This iterative process converged in one step for the background and just a few steps for the position.

We used a nonlinear least squares minimization program to find the map that best fit the image data for each set of coupled Hapke parameters. These parameters, along with the final  $\chi^2$ , are listed in Table 2. Note that the value of  $\chi^2$  listed is the amount

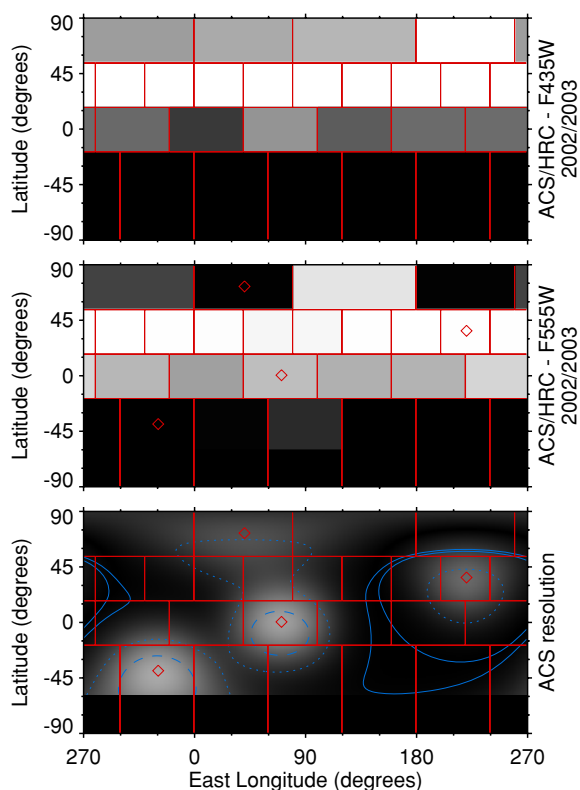


**Figure 3.** Free-parameter gridding for Charon map solution. The surface of Charon is broken up into a grid where each outlined zone is one free parameter of single-scattering albedo and is based on an underlying  $18 \times 10$  array. The albedos shown are from the final fitted results. Blocks of elements in the array are grouped together to more closely match the spatial resolution on the surface and the constraints possible from the data. The bottom segment of the plot shows a point response of the map calculation. The contours are shown at a change of 0.001 (solid), 0.02 (dotted), 0.04 (dashed), and 0.06 (dash-dotted) in single scattering albedo after the spherical smoothing from an initial change of 0.1 in the map grid. The diamonds mark the location in the map where the change was inserted. This result gives an indication of the spatial resolution possible with this map reconstruction.

(A color version of this figure is available in the online journal. Supplemental digital source data and software is available online.)

per degree of freedom. We also weighted each image data value by its expected uncertainty assuming photon counting statistics. Since the FOC is a photon counting instrument, this assumption should be very good. Each of these sets (A–F) of Hapke parameters worked equally well in deriving a map according to the final goodness-of-fit statistic. We have arbitrarily chosen set A as our adopted set of parameters. This choice was guided by picking a set that falls in the middle of the range of valid parameters. The visual appearance of the fitted maps is the same, further demonstrating that the fitting process reaches the same result for a different set of fitting parameters.

### 3.4. ACS/HRC Model

The reference solar flux at 1 AU for the ACS model was  $170.384 \text{ erg cm}^{-2} \text{ s}^{-1}$  for the F435W filter and  $187.463 \text{ erg cm}^{-2} \text{ s}^{-1}$  for the F555W filter and was derived by integrating over the instrumental response from the solar spectrum of Colina et al. (1996). It was not practical to fit all six sets of Hapke parameters so we fitted these data using only set A. Unlike the FOC map, the ACS model did not discretize the sky-plane position.

The PSF used was generated by TinyTim version 6.2 (Krist 2004) using our independently fitted focus position ( $z_4$  Zernike

term) for each image. This numerical PSF was calculated at a factor of 3 finer interval than the idealized pixel scale so that the PSF was interpolatable. At the very end of the calculation, the numerical PSF and the model image were passed to the final stage (tiny3) of the TinyTim package that then applies the geometric distortion across the entire image. It is this step that consumed virtually all of the CPU time for the fitting process.

The focus fitting process used discretized focus values that scanned over the range of  $-1 \leq z_4 \leq 1$  at a step size of 0.001 to find the overall lowest  $\chi^2$  for each image. A small fraction of the images did not yield appropriate fitted values for focus. These special cases were assigned a non-fitted focus value that was determined by visual inspection and evaluation of the focus trends from adjacent images where the focus fit worked more convincingly.

The complete fitting process involved iterating between adjusting the map, position, and telescope focus. The positions and focus were fit just a few times during the entire process. The bulk of the fitting work was iterating on the map. Given a map, the fit for focus and position was relatively quick (less than an hour of CPU time). The map fitting step was very slow given the computational cost of the image distortion calculation. Convergence from a given starting point took roughly 16 weeks on a 20-node parallel computing cluster. A limited number of starting values were processed to help constrain the uncertainty on the final map product. These starting values were a uniform map with  $w = 0.8$  and a map derived from the FOC results. There were three sets of data fitted: (1) the first six visits in time order, (2) the last six visits, and (3) all the visits together. The visits were scheduled such that the first six were scheduled at the end of the 2002 apparition of Pluto with a  $60^\circ$  longitude spacing. The other six visits were in the first half of the 2003 apparition with a  $60^\circ$  longitude spacing but shifted by  $30^\circ$  from the other set of visits. As the fitting progressed, other intermediate maps were generated by using a converged map from a different data set or starting point. In all, we generated partially converged maps for 11 cases for the *B* (F435W) map and five cases for the *V* (F555W) map. Despite the many cases tried, only one solution could be brought to a final converged solution due to changes in calibrations and fitting technique that crept in during the long fitting process. We present here the results from fitting all the data in each filter that started from a uniform albedo map. The other partially converged results are used only to confirm the stability of the fitting process.

The fitting process did a very good job of matching the model image to the data. Some examples of the data and the image residuals are shown in Figure 4. Two representative images and their residuals are shown for each visit and each filter. The choice of pattern step number was made to highlight differences (or lack thereof) caused by dithering. The residuals are not completely random and point to systematic problems unique to each visit. Jitter has been ruled out as a contributing factor but many other possibilities remain, such as charge diffusion in the CCD and imperfections in the size of the core of the PSF.

## 4. MAPS

### 4.1. Pluto

Figure 5 shows the final maps of Pluto's surface from our new analysis. For comparison, the map from Buie et al. (1992) is shown at the same scale (top panel). To allow the visual comparison of the maps, each has been converted to

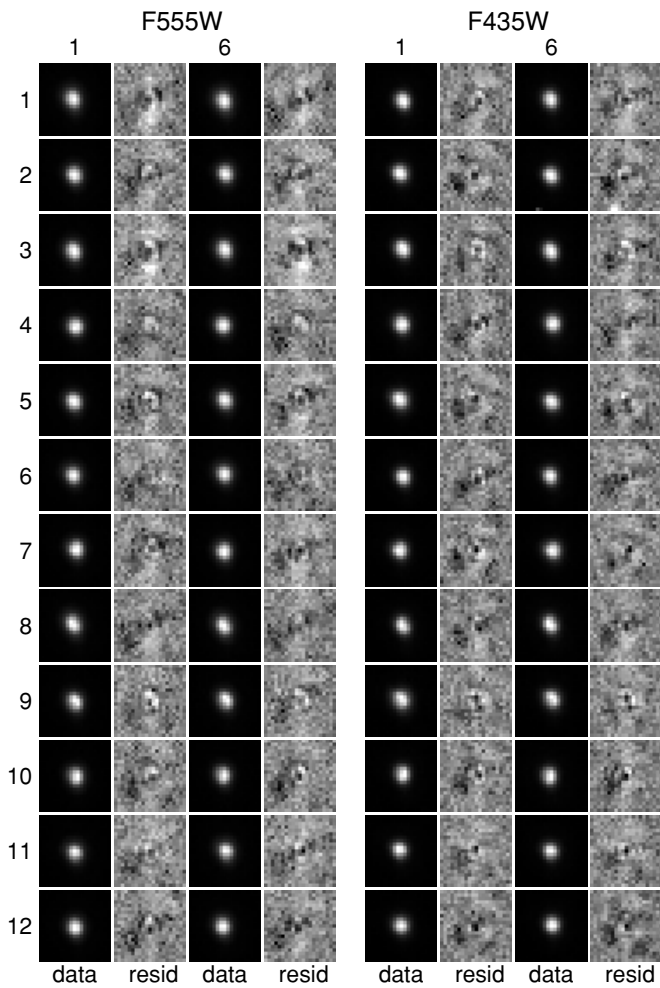


**Figure 4.** Sample post-fit image residuals. This figure shows a small subset of the F555W image data (left) and F435W data (right). The visit number is indicated on the far left. The image columns labeled “data” show the original image data of Pluto. Each visit consisted of 16 images in each filter. Here we show just two images corresponding to pattern step numbers 1 and 6 (labeled at the top). To the right of each data image (labeled “resid” at the bottom) is an image of the post-fit residuals after the model image is subtracted from the data. The residual images are shown in units of a standard deviation and is scaled to a constant range of  $\pm 3.0\sigma$  (a posteriori confidence level).

bidirectional reflectance with normal illuminance and  $1^\circ$  phase viewing angle.

The F410M FOC map (middle panel in Figure 5) represents a significant improvement over the previous reduction from SBT. The map is an absolutely calibrated product and does not suffer from the limb artifacts noted in the prior reduction. Also, the amount of detail seen in the map is somewhat higher. However, the large-scale features in the map are the same as in SBT, such as the large dark province at  $90^\circ$ – $120^\circ$  longitude and the bright equatorial region near  $180^\circ$  longitude.

In comparison, the F278M FOC map (second panel from the top in Figure 5) has regions markedly different from the SBT map as well as the new F410M map. The basic structure of dark and light provinces in the equatorial zone are repeated but the north pole and the southern terminator look quite different between the two colors.

The new F435W ACS/HRC map (second panel from the bottom in Figure 5) provides the closest comparison map relative to the prior F410M FOC map. The spatial resolution of the ACS data is slightly lower making an exact temporal comparison difficult. Nonetheless, the data suggest a general brightening of

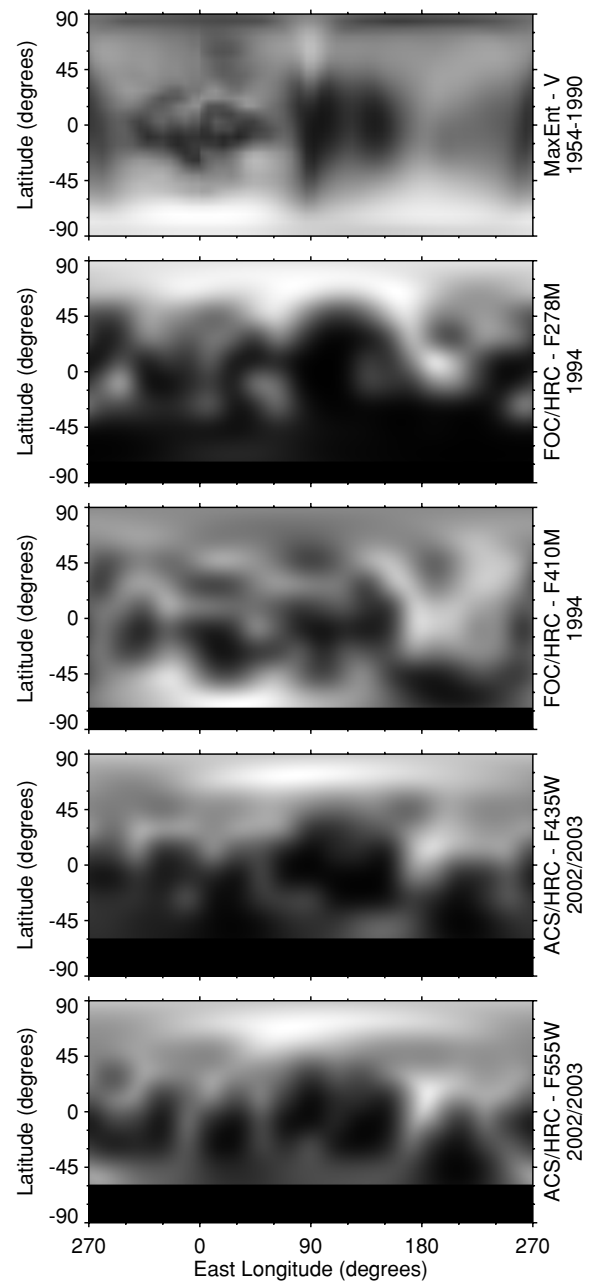


**Figure 5.** Bidirectional reflectance maps of the surface of Pluto. The top panel shows the V-band map from Buie et al. (1992) that were based on mutual-event and rotational light curve data labeled as “MaxEnt.” The second panel shows the map from 1994 based on the re-analysis of the *HST*/FOC data. The third and bottom panels show the B and V maps based on the *HST*/ACS data. The black stripe at the bottom is the region hidden from view at the epoch of these maps. All maps are shown as  $I/F$  from 0 to 1.2 (black to white) at a normal illuminance and  $1^\circ$  phase angle.

(Supplemental digital source data and software is available online.)

the north polar region as well as a darkening of the southern terminator. The light curve results from Paper I clearly indicate a global darkening at these blue wavelengths but looking at these maps it is not possible to point to a specific area that could be responsible for the change.

The F555W ACS/HRC map (bottom panel in Figure 5) looks very similar to the contemporaneous blue map. The same large-scale light and dark features are evident but there are some regions where the agreement between the two filters is not as tight. In particular, the southerly regions from  $270^\circ$  to  $0^\circ$

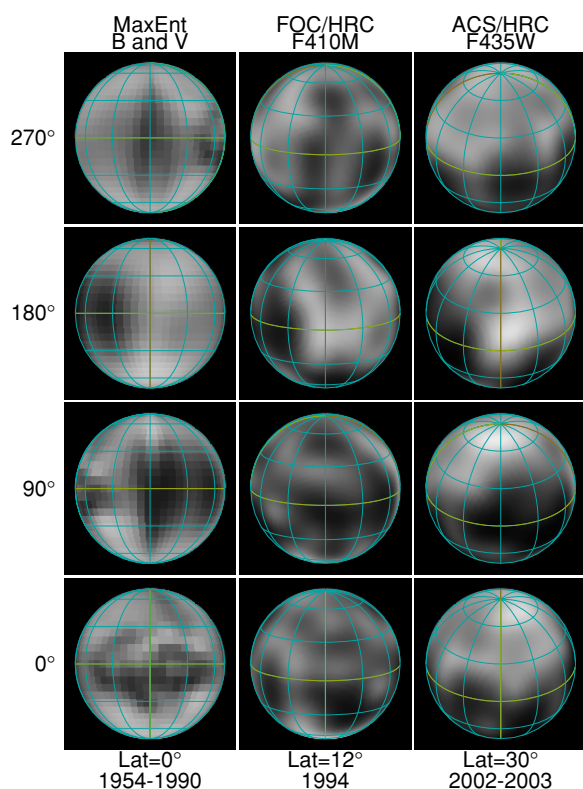


**Figure 6.** Rendered globes of Pluto. All globes depict the bidirectional reflectance or  $I/F$  at  $1^\circ$  phase angle as seen from the central longitude listed on the left. Each map product is shown at the sub-Earth latitude where the data are best constrained. Each column is labeled with the latitude and time range of its constraining data. The left column, labeled “MaxEnt” is from the map published in Buie et al. (1992). This map has a variable spatial resolution that peaks for the sub-Charon hemisphere ( $0^\circ$  longitude). The middle column is from the FOC F410W map and the right column is from the ACS F435W map. The yellow lines mark the equator and prime meridian, while the orange line marks  $180^\circ$  longitude. The grid spacing of the cyan lines is  $30^\circ$ . The images have been scaled to preserve the relative photometry between all rendered globes for a given map.

(A color version of this figure is available in the online journal.)

longitude appear to be generally redder than the rest of the surface. The color light curve results from Paper I tell a slightly different story in that the least red longitude is at  $210^\circ$  and the most red longitude is at  $150^\circ$ . The spatial variation of color is clearly not easy to describe but these results clearly indicate that there are real variations.

Rectangular map projections are useful tools but suffer from spatial distortions, especially near the poles. Another way to view the results is shown in Figure 6 where we display globes rendered from these maps at four principal sub-Earth longitudes. This figure compares maps from three epochs showing each at the mean sub-Earth latitude for the respective data set. The changing aspect during the period of observation is quite evident. Also seen here is the degree of foreshortening that affects how maps are constrained at the north pole, particularly in the MaxEnt and FOC data sets. These images also make it clear that the bright southern polar region is no longer visible and we are left to wonder what changes may be taking place there.

Perhaps just as striking in this rendering is that the north pole appears to be brighter now than in the recent past. Such a brightening is somewhat surprising given that this is the region that is seeing a substantial increase in solar insolation and a common expectation is that this increase in energy deposition

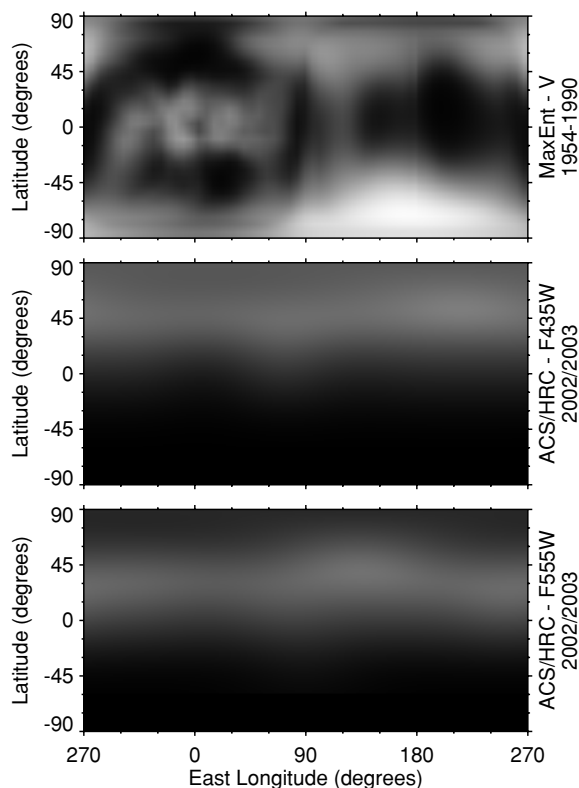


**Figure 7.** Bidirectional reflectance maps of the surface of Charon. The top panel shows the  $V$ -band mutual-event based map from Buie et al. (1992). The middle and bottom panels show the  $B$  and  $V$  maps based on the *HST*/ACS data. The black stripe at the bottom is the region hidden from view at the epoch of these maps. All of the structure in the older map from  $90^\circ$  to  $270^\circ$  is spurious and was caused by correlations between the Charon and Pluto maps during the photometry inversion process. The equatorial structure around  $0^\circ$  longitude could still be of value but the resolution of the new maps is too low to permit a useful comparison.

(Supplemental digital source data and software is available online.)

rate should darken the surface, although Grundy & Stansberry (2000) identified some mechanisms likely to lead to brightening, at least initially.

#### 4.2. Charon

The newly derived maps for Charon are shown in Figure 7 with a comparison against the mutual event based map from Buie et al. (1992). The spatial resolution should be similar to that of the Pluto maps, but the smaller size of Charon means the amount of information on the map is a factor of 4 lower by area alone. Also, Charon’s smaller size leaves this technique open to more difficulties with systematic errors in the fitting process. As a result, these maps are considered to be tentative and are presented primarily for completeness. Taken at face value these maps are certainly consistent with the light curve, in that little longitudinal structure is seen. The latitudinal structure in the maps is intriguing but not entirely consistent with the light curve record. As was seen in Paper I, the Charon light curve between 1992 and 2002 is essentially identical for both the  $V$  light curve and the mean color. However, the slight difference in mean color noted in Paper I, attributed to photometric transformation errors or phase-reddening, is qualitatively consistent with these maps showing latitudinal trends. Figure 8 shows the ACS F435W map rendered as globes. At this resolution, there is very little albedo structure to be seen.

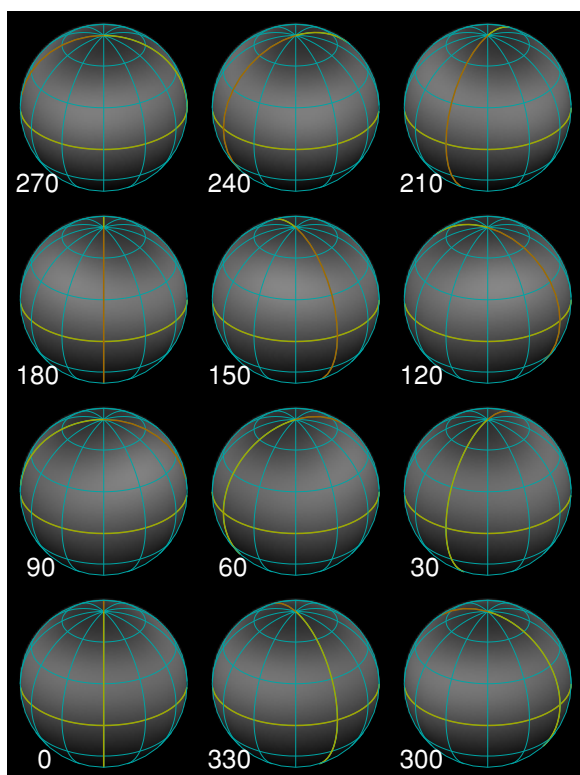


**Figure 8.** Rendered globes of Charon. All globes depict the bidirectional reflectance or  $I/F$  at  $1^\circ$  phase angle from the ACS F435W map at the mean latitude ( $30^\circ$ ) in 2002/2003. The central longitude of each globe is given to the lower left. The yellow lines mark the equator and prime meridian, while the orange line marks  $180^\circ$  longitude. The grid spacing of the cyan lines is  $30^\circ$ . The images have been scaled to preserve the relative photometry between all rendered globes. The sequence of globes lets you see the satellite as it rotates (longitude decreasing with time).

(A color version of this figure is available in the online journal.)

The MaxEnt maps for Charon have long been a puzzle. Buie et al. (1997) pointed out that the map could not be correct since it predicts the wrong light curve. However, this categorical denial of the entire map may have been premature. Certainly the portion of the map from  $90^\circ$  to  $270^\circ$  is not useful in the MaxEnt map because that area was constrained by combined light photometry (Pluto+Charon). However, the sub-Pluto hemisphere, centered at  $0^\circ$ , is directly constrained by mutual event light curve data and as such should contain some measure of truth. The MaxEnt map does contain an element of latitudinal variation similar to that seen in the ACS maps suggesting that the latitudinal trend could be real.

## 5. DERIVED MAP PRODUCTS

The maps presented in the previous section are the direct result of the fitting process and represent the primary result of this work. There are other secondary results that come from further analysis of the maps or the statistical output of the fitting process.

### 5.1. Albedo Change with Time

The light curve results in Paper I already indicate a significant change at a global level for Pluto's albedo versus time. We examined the fitting results in search of a signature that could be related to this change. Figures 9 and 10 attempt to show the goodness-of-fit on an image combined with a sensitivity

matrix that shows how each image constrains (or not) each free parameter. The details of the constructed image are in the caption, but these complicated data products are better viewed from a larger perspective. In this rendering, mid-level gray corresponds to either a perfect fit of the model to the data or no constraint at all. The diagonal gray stripes basically show where given tiles in the map are not visible as Pluto rotates. The areas in between show the constrained regions. If a model image is too dark relative to the data then that pixel will be darker than a perfect fit. If the model image is too bright then you see a brighter region.

Looking at the information for the F435W data in Figure 9, one sees a striking light/dark pattern between odd and even visit numbers. Recall that the odd visit numbers were taken as a set in the first half of Cycle 11 and that the even visit numbers were in the latter half of the cycle. In this view, it is easy to see that the model trends from being too dark early in the cycle to being too bright late in the cycle, relative to the data. There is clearly some longitudinal structure to the temporal variation since the pattern is not perfect. When compared to the F555W result in Figure 10, there are some visits with systematic errors (especially visit 9) but the overall temporal pattern seen with F435W is absent. Keep in mind that the forward model includes all purely geometric changes that occur during the observations. Since the model includes geometric change but not temporal change, the lack of temporally structured residuals in the F555W data is consistent with a static map during Cycle 11. The temporally structured residuals in the map fits to the F435W data clearly point to a failure of the model to track the data as it did for F555W. The most likely interpretation of these residual patterns is the existence of unmodeled temporal variations in albedo during the year.

### 5.2. UV Color Map

The FOC maps were intended to test for ice purity by obtaining data in the ultraviolet. Figure 11 shows a false-color rendering of the FOC maps. In this figure, neutral reflectance would be white (or gray). Blue regions indicate where the  $I/F$  is higher in the UV than in the visible. Red regions indicate UV dark areas. The north polar regions and the bright equatorial spot at  $180^\circ$  longitude are UV bright, consistent with clean ice. Possible explanations for a region being UV dark include the accumulation of photolytic or radiolytic residues in the polar ice or removal of ice exposing these materials in an ancient substrate.

### 5.3. Optical Color Map

One of the goals of this program was to attempt color maps of the surface of Pluto. With only two wavelengths sampled, it is not possible to directly create a true color image. However, the spectrum of Pluto at visible wavelengths is known to be free of any strong absorption features making it feasible to synthesize a plausible facsimile. Given that the continuum absorbing reddening agent is expected to be related to high-order hydrocarbons, we created a simple spectral mixing model using a gray reflector with an extreme-red laboratory tholin spectrum. The tholin spectrum choice was dictated by needing something as red as the reddest point in the Pluto maps. The base spectrum we used was the Triton tholin of Khare et al. (1994) computed for a  $4 \mu\text{m}$  grain size. We do not attach any particular significance to the details of the synthetic spectrum except that it represents something close to an actual spectrum for a plausible surface component.

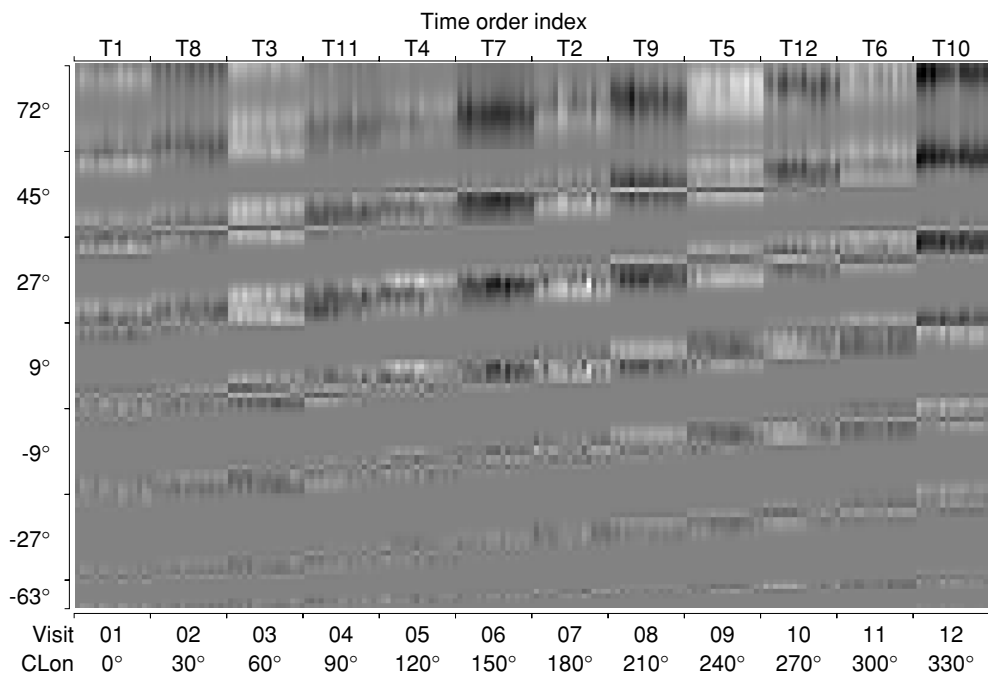


**Figure 9.** Per-image goodness-of-fit for the F435W model fit to image data. The horizontal axis is organized first by visit and then by image number within the visit. The vertical axis is organized by the map free parameters with spin-north at the top and spin-south at the bottom. The left axis denotes the central latitude of each strip of the map and the tick marks denote the span of the map values at that latitude. Within a latitude band the map values are organized from 0° to 360° longitude. The bottom axis labels the span of each visit-by-visit number and targeted central meridian longitude. The top axis shows the index ordered by time with T1 being the first visit and T12 being the last visit in the set of observations. Each column in this presentation shows the trends for a single image, while each row shows how the entire data set constrains each map value.

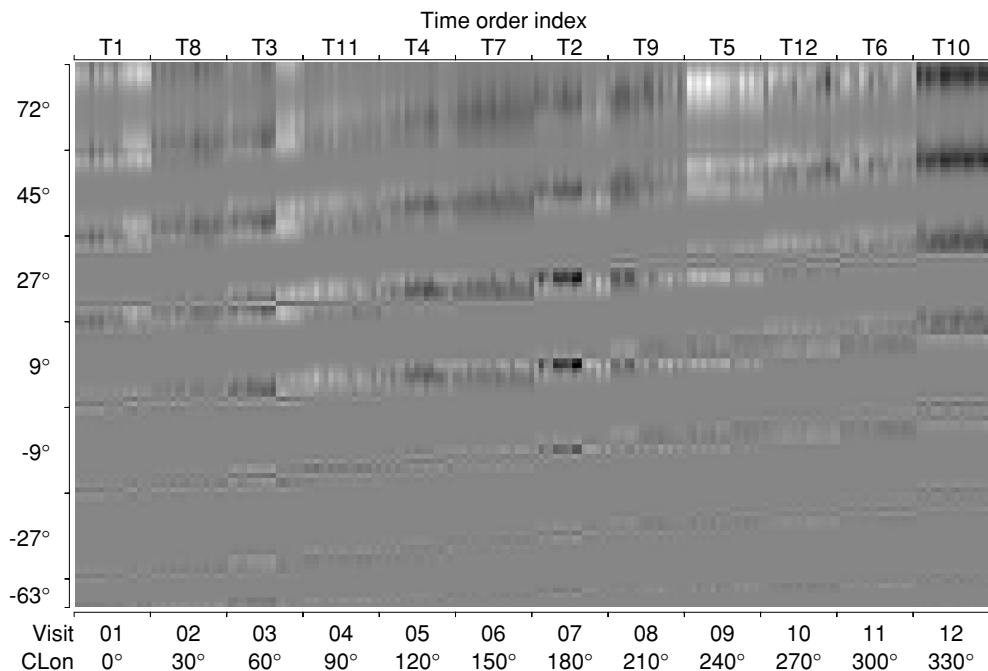


**Figure 10.** Per-image goodness-of-fit for the F555W model fit to image data. The horizontal axis is organized first by visit and then by image number within the visit. The vertical axis is organized by the map free parameters with spin-north at the top and spin-south at the bottom. The left axis denotes the central latitude of each strip of the map and the tick marks denote the span of the map values at that latitude. Within a latitude band the map values are organized from 0° to 360° longitude. The bottom axis labels the span of each visit-by-visit number and targeted central meridian longitude. The top axis shows the index ordered by time with T1 being the first visit and T12 being the last visit in the set of observations. Each column in this presentation shows the trends for a single image, while each row shows how the entire data set constrains each map value.

We synthesized a color map by solving for the gray/tholin mixing ratio and gray albedo that would match the observed bidirectional reflectances in the F435W and F555W filter maps from Figure 5. This simple model gives us a spectrum for each

point on the map. Using the formalism discussed by Young (1984), we converted these spectra to CIE color indices and in turn to their RGB equivalents. The resulting color map of Pluto is shown in Figure 12 and a display of rendered globes

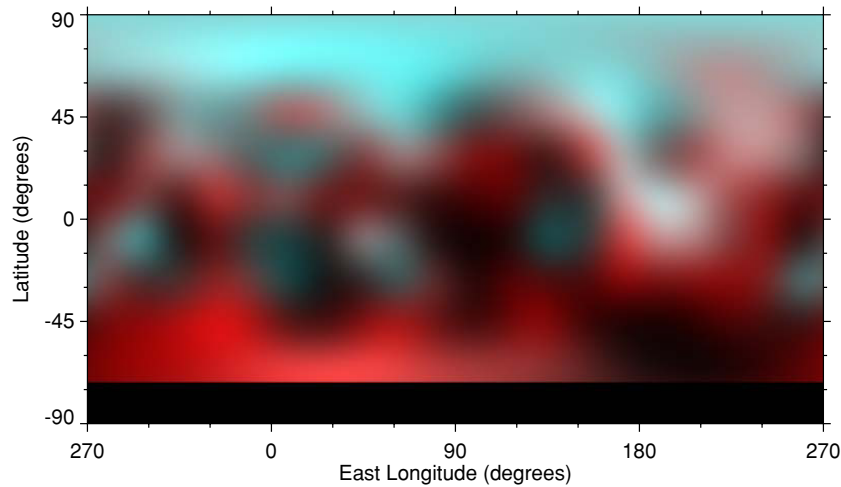


**Figure 11.** False color map of the surface of Pluto. This image combines the UV and VIS maps from the FOC data into a false color representation where blue and green are equal to the UV map (shades of cyan) and red is equal to the VIS map. The black stripe at the bottom is the region hidden from view at the epoch of these maps.

(A digital version of this image is available online.)

is shown in Figure 13. As one might expect from the light curve observations, the general cast of the surface color is widespread but it is equally apparent that Pluto's surface colors are variegated.

To further examine this color map product, we generated a number of color distribution plots. For these plots, we binned the entire surface into 80 equal area bins with approximately square tile footprints. The tile area was  $2.1 \times 10^5 \text{ km}^2$  or roughly equivalent to a  $460 \times 460 \text{ km}$  patch. Within each tile we averaged the bidirectional reflectances at F435W and F555W and then converted to CIE ( $x, y, Y$ ) just as we did for the map.

The first distribution is plotted in Figure 14 where the points on the surface are shown against the same portion of the CIE chromaticity diagram as Young (1984). For reference, other "colorful" example surfaces are plotted such as different regions on Io, (5145) Pholus, and Mars. The chromaticity for Charon is also shown along with global values for Pluto in 1992 and 2002. Though the global color change is substantial, it pales compared to the apparent range of color on the surface of Pluto. Note that some points on Pluto approach the pure-white point on the diagram (labeled W) but nothing is bluer than white. The point labeled "red" shows the reddest color we can synthesize using our tholin template spectrum. Mathematically, a solution outside the range of W–red is possible but such solutions are not physical for our simple mixing model and also not seen in our color decomposition. The points on the figure are also shown in color with an RGB approximation of how that chromaticity would appear. The points are also plotted against a 30% neutral gray background to prevent a spurious shift in the perceived color of the points. The color range is quite strong in the context of planetary surfaces and yet the true range of perceived color is more subdued.

This analysis shows that Pluto is significantly less red than Mars and much more similar to the hues seen on Io with a slightly more orange cast. Of course, our palette of available colors is limited by the two-component mixing model. If there are other spectral units we would expect more color diversity perpendicular to the locus of points in Figure 14.

The chromaticity diagram shows the range of colors present on the surface but does not aid in seeing any other patterns. Figure 15 takes the same points and shows the distribution of color as a function of albedo. In this case, we have plotted

the F555W value against the F435W/F555W reflectance ratio. Again, the points have the color and brightness corresponding to their CIE values and are plotted against a 30% neutral gray value. The global color is shown with a line labeled with P2002. The color distribution shows a clear trend of increasing color diversity with decreasing albedo. This diversity argues strongly that the dark regions are not compositionally homogeneous as is usually assumed. These regions may span the range from more neutrally colored carbon-rich material to the extreme red of tholin-rich material. Finally, the brightest regions have a color more neutral than the global color while still being quite distinct from white.

The next obvious question is to understand the spatial distribution of color units. Figure 16 shows the same points plotted as latitude as a function of the F435W/F555W reflectance ratio. This distribution also shows a trend of increasing color diversity moving away from the north pole. This plot also clearly shows the most neutral and most red samples are all at the southernmost extremes of the data. These samples are the most poorly determined and this extreme range is probably spurious. Still, the trend remains intact even without the southernmost band. Also seen here the brighter terrains tend to be north of the equator.

Figure 17 shows the color distribution with longitude. Here, there do not seem to be any strong trends. This result is consistent with the lack of strong color variation with rotation that has been noted for decades and most recently shown in Paper I.

#### 5.4. Center-of-body Versus Center of Light

The eccentricity of Charon's orbit has generated much interest over the years (Tholen & Buie 1997). Results from orbit fitting based on mutual event data never produced a convincing measurement largely because of the coincidental alignment of the line of apsides with the line of sight. A spherical object with a uniform albedo at zero phase will have a center of light (COL) or photocenter that will be coincident with the center of body (COB). However, a non-uniform map can lead to a COL shift relative to the COB that could manifest as a false eccentricity for a tidally locked object like Charon. The first epoch of observations from *HST* in 1992 raised the possibility of a non-zero eccentricity but also could not determine a definitive value because the size of correction for photometric center of

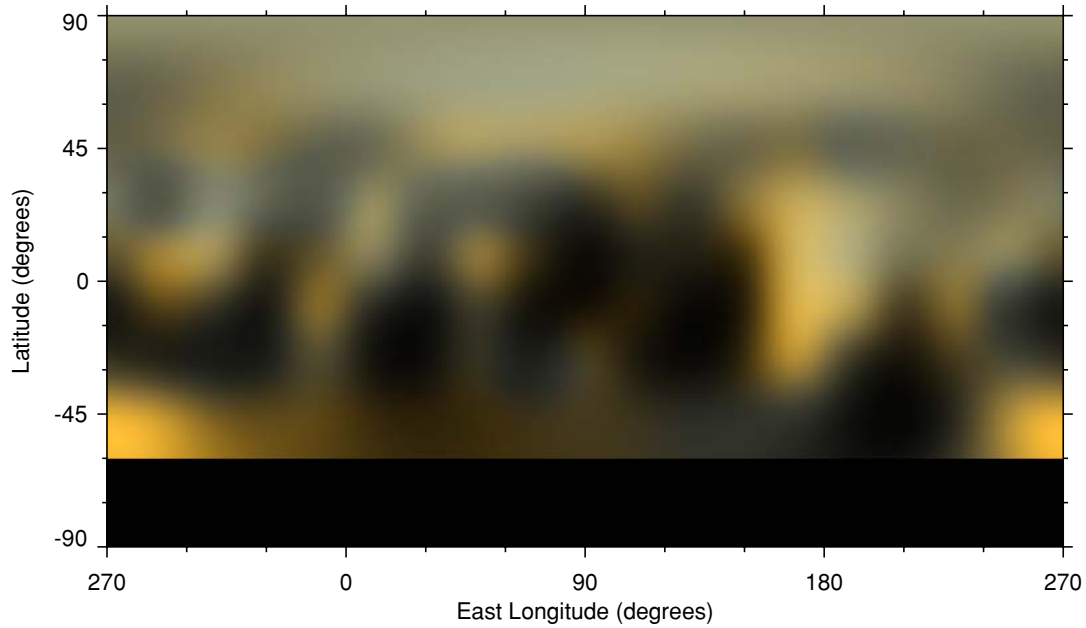


**Figure 12.** Synthesized true-color map of the surface of Pluto. The F435W and F555W maps constrain a two-parameter mixing model of a gray component and a red tholin component. The resulting spectrum is then decomposed into CIE color values and then converted into RGB for display. The black stripe at the bottom is the region hidden from view at the epoch of these maps.

(A digital version of this image is available online.)

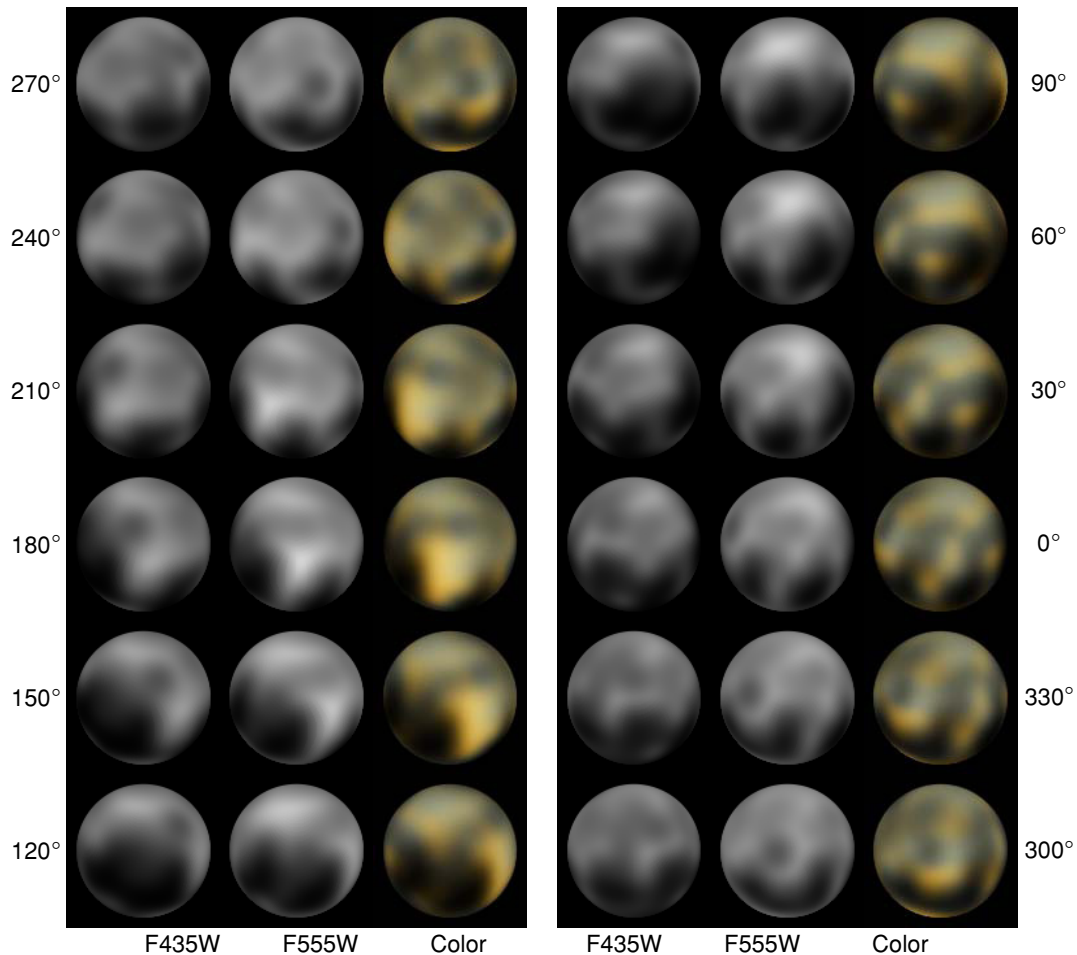


**Figure 13.** Rendered globes of Pluto with color. All globes depict the bidirectional reflectance or  $I/F$  at  $1^\circ$  phase angle. The 12 longitudes with ACS imaging are shown in two columns. From left to right at each row in the columns there is a globe from the F435W map, from the F555W map, and finally an approximation of a true-color image of the surface. All images are rendered at a sub-Earth latitude of  $31^\circ$  to match the aspect seen during the ACS observations.

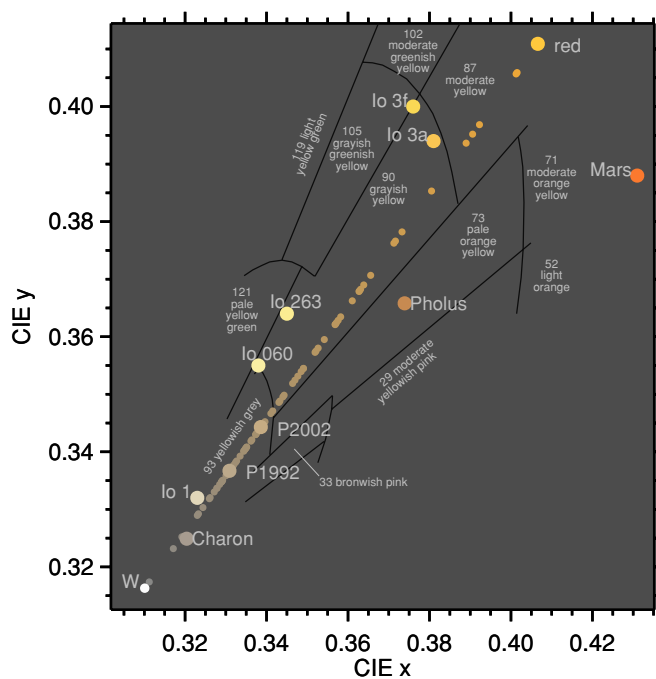


**Figure 14.** Distribution of terrain color on Pluto. This plot shows the portion of the CIE chromaticity diagram that is relevant to the range of surface color on Pluto plus some of the more colorful solid surfaces in the solar system. The background in the plot is set to a 30% gray value to facilitate the perception of the displayed colors. The faint black lines on the background show the color boundaries from the translation of standard Munsell color domains. The points labeled as lo show different regions (1, 3a, and 3f as described by Young 1984) and different global colors (leading hemisphere, 60° and trailing hemisphere, 263° longitude from the spectra of Spencer et al. 1995). Also included is a color for Mars using the average spectrum for the bright terrains from Mustard & Bell (1994). The dots along the diagonal show the colors for various areas on the surface of Pluto. Also shown are two reference “colors” for white (W – Illuminant C) and “red” (see the text for details). All symbols are plotted with the color of the point on the chromaticity diagram using the highest illuminance value (Y) that does not saturate any of the RGB values. A constant value of  $Y = 0.53$  is used for all Pluto terrains to prevent color saturation. The point labeled “P2002” is the global averaged color for Pluto in 2002 and “P1992” shows the globally averaged color in 1992. All values with  $x > 0.34$  correspond to a NBS color value of 90 “grayish yellow.” Lower values of  $x$  lie in region 93 “yellowish gray.” The area represented by each point is  $2.1 \times 10^5 \text{ km}^2$  (1/80 of total surface area).

(An enhanced color version of this figure is available in the online journal.)

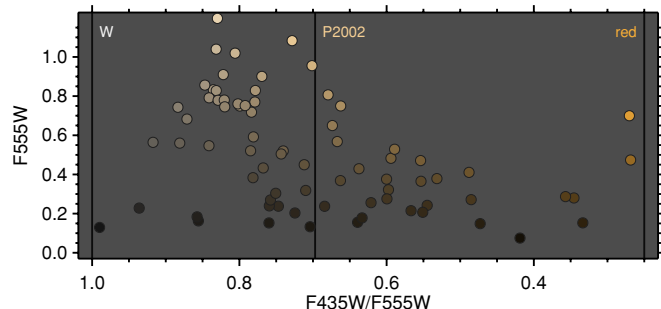


**Figure 15.** Distribution of terrain color on Pluto vs. albedo. The  $F555W/F435W$  value is plotted as a function of the  $F435W/F555W$  flux ratio (see the text for details). The background of the plot is a 30% gray value. The color and intensity of each point on the plot are plotted according to its  $(x, y, Y)$  CIE chromaticity value. The vertical lines are located at the white point (W), the Pluto global average color (P2002), and “red” (the same points as shown in Figure 14). This plot clearly shows the increasing color diversity with decreasing brightness and the brightest regions are all more neutral than the average.

(An enhanced color version of this figure is available in the online journal.)

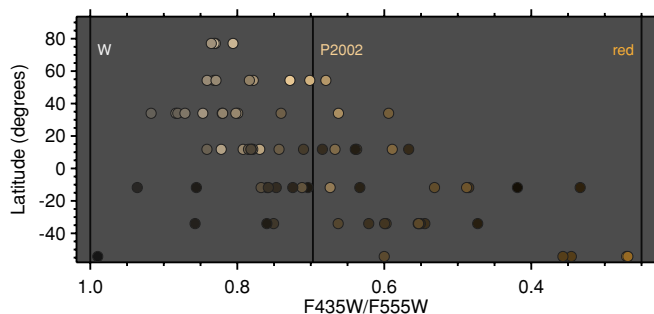


**Figure 16.** Distribution of terrain color on Pluto vs. latitude. Latitude is plotted as a function of the  $F435W/F555W$  flux ratio (see the text for details). The background of the plot is a 30% gray value. The color and intensity of each point on the plot are plotted according to its  $(x, y, Y)$  CIE chromaticity value. The vertical lines are located at the white point (W), the Pluto global average color (P2002), and “red” (the same points as shown in Figure 14). Color diversity is higher in the southern hemisphere. Note that the most extreme red terrains and the point closest to white/gray occur at the southernmost latitude band where the uncertainties are the largest due to extreme foreshortening.

(An enhanced color version of this figure is available in the online journal.)

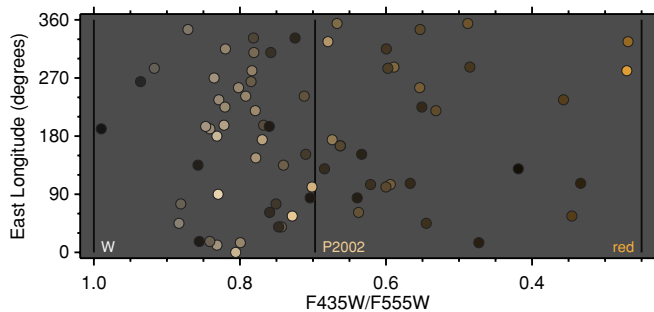


**Figure 17.** Distribution of terrain color on Pluto vs. longitude. East longitude is plotted as a function of the  $F435W/F555W$  flux ratio (see the text for details). The background of the plot is a 30% gray value. The color and intensity of each point on the plot are plotted according to its  $(x, y, Y)$  CIE chromaticity value. The vertical lines are located at the white point (W), the Pluto global average color (P2002), and “red” (the same points as shown in Figure 14). No strong systematic variations are evident as might be expected from the weak variation in color seen in the rotational light curve.

(An enhanced color version of this figure is available in the online journal.)

Pluto’s disk to the COB was comparable and synchronous with the effects of orbital eccentricity.

Our data set is the first that is able to solve for the center of the disk directly while simultaneously fitting for the map. The position for Charon was fitted using a uniform albedo disk and then later with a surface map. These observations are so far the highest precision astrometry data set for the orbital motion of Charon. The uniform-disk astrometric measurements have already been analyzed and published in Buie et al. (2006) and Tholen et al. (2008) and are responsible for a convincing measurement of the orbital eccentricity. From the alternate map solutions, we see induced variations in the COL–COB offset for Charon that is 20–40 km, well below the scatter in the orbit fits and thus do not believe the astrometry is improved by using a map in the positional fitting.

Figure 18 shows the COL–COB offset for the current epoch. This map should permit the calculation of reasonably accurate offsets in the future as the sub-Earth latitude continues to move away from the equator. Corrections to earlier data sets will require filling in the gaps in the southern hemisphere of the map. This effort is possible but must be done with care since an error in the missing albedos will lead to system errors in the

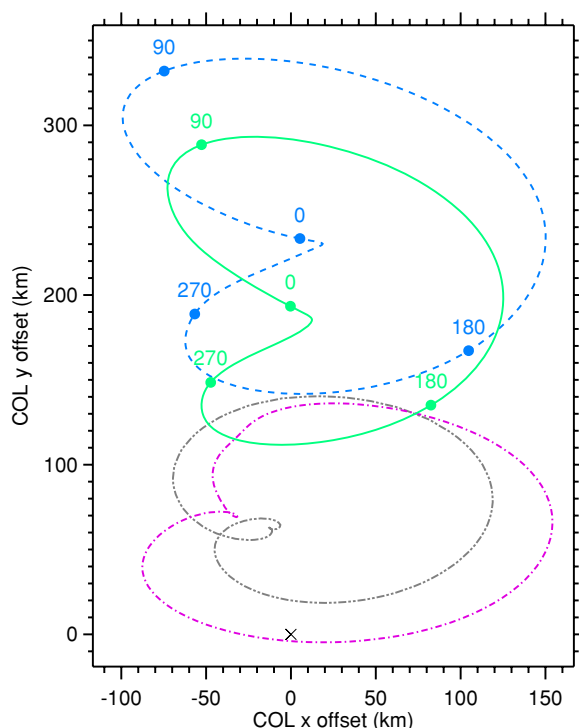


**Figure 18.** Position of Pluto’s COL relative to the COB. The solid (green) curve is for F555W and the dashed (blue) curve is for F435W. The labeled dots indicate the sub-Earth (east) longitude. The position of the COB is marked with an X. The Pluto COL based on the FOC VIS map is indicated with the dot-dotted (magenta) line. The MaxEnt map COL is indicated with the dot-dotted-dashed line. These calculations are all based on the mean sub-Earth latitude ( $30^\circ 0$ ) during the ACS observations (2002/2003) and a  $1^\circ$  solar phase angle. This coordinate system is Pluto-centric with the projected angular momentum spin axis in the  $+y$  direction.

(A color version of this figure is available in the online journal.)

astrometric correction. Enough data have been collected to do this work but it is outside the scope of this paper.

### 5.5. Center of Mass versus Center of Light

Given these maps and the light curves, we can now also compute an accurate offset from the photometric center of the entire Pluto system to the barycenter. This is an obvious correction that should be made when analyzing astrometry of the Pluto–Charon blended object. In principle, this correction varies with orbital longitude, orbital latitude, solar phase angle, and wavelength of observation. Figure 19 illustrates the combined system correction projected on the plane of the sky at the epoch of the ACS data for a common solar phase angle. A simpler view of the same information is shown in Figure 20 where the correction is reduced to a one-dimensional quantity. The offset is largely in the direction of Charon, so by ignoring offset perpendicular to the Pluto–Charon line it is easier to see the size and variation of the photometric effect. At the current distance of Pluto, the separation is roughly 1 arcsec at maximum elongation. Nonetheless, this figure illustrates the amount of variation within one rotation and an example of the error one would make by ignoring the effective wavelength of the astrometric measurement. This effect may make little difference in the interpretation of a large data set such as might be used to determine the orbit of the center of mass of the Pluto system. But this effect can be quite important when attempting high-precision astrometry for the purposes of predicting stellar occultations by one of the objects in the system. Note that these

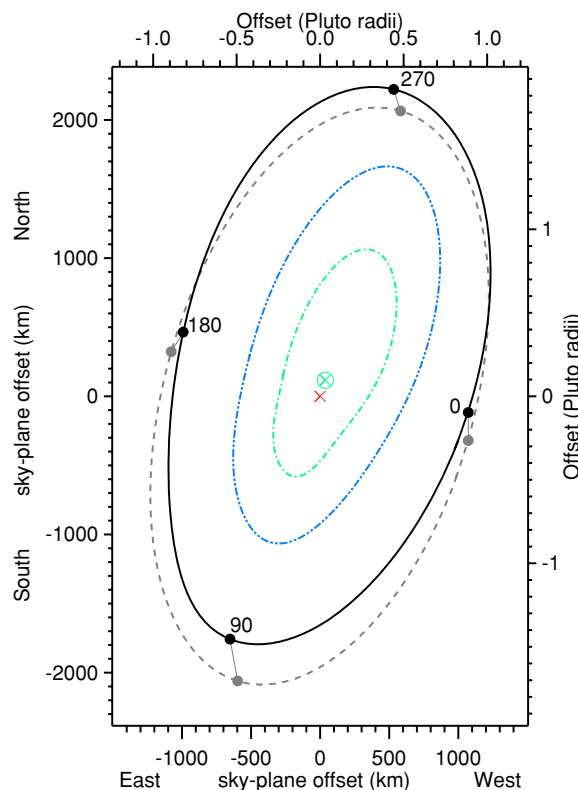


**Figure 19.** System COL position relative to the system barycenter for the 2002/2003 epoch (J2000 coordinate system). The plot is centered on the Pluto–Charon barycenter (red X) using a Charon/Pluto mass ratio of 0.1166 (Tholen et al. 2008). The dashed (gray) curve shows the motion of the COB of Pluto over one orbital period for Charon. The solid black curve is the position of the Pluto photocenter using the F555W map. Superimposed on these two curves is a labeled point denoting the sub-Earth longitude at that point in the orbit (with a gray line connecting the related points). The dot-dashed (green) curve is the position of the combined Pluto/Charon photocenter which includes COL–COB offsets as well as the differences in reflected flux from the two bodies (using the F555W map and  $1^\circ$  phase angle). The three-dot-dashed (blue) curve represents the combined light photocenter in the F435W filter, again at  $1^\circ$  phase. The circled X (green) shows the average position of the system V-band photocenter at (36, 110) km from the barycenter. The B-band average position (not shown) is at (110, 137) km.

(A color version of this figure is available in the online journal.)

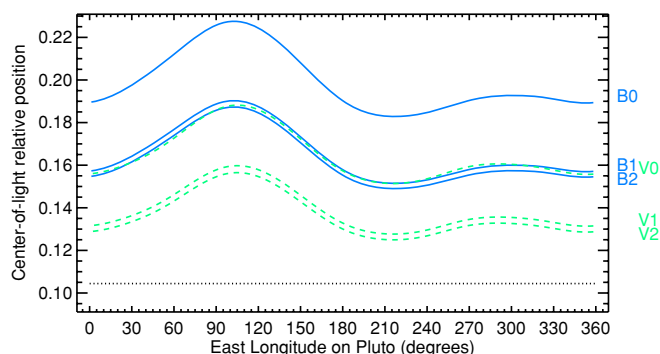


**Figure 20.** Position of the system COL from the center of Pluto divided by the apparent separation between Pluto and Charon. The solid (blue) curve is the position of the system photocenter at blue (F435W) wavelengths. The dashed (green) curve is the position at green (F555W) wavelengths. For each color, there are three curves computed at  $0^\circ$ ,  $1^\circ$ , and  $2^\circ$  solar phase angle (labeled on the right by filter and phase angle). The horizontal dotted line at the bottom indicates the position of the system barycenter at a position of 0.104. The mean F435W correction is 0.165 and the median is 0.160, at  $1^\circ$  solar phase angle. The mean F555W correction is 0.140 and the median is 0.136, again at  $1^\circ$  solar phase angle.

(A color version of this figure is available in the online journal.)

results cannot be extended to wavelengths longer than *V* band. Longer wavelengths are affected by spectrally active ices that can significantly perturb these COL–COB offsets and a loss of accuracy can be expected.

## 6. DISCUSSION

Intercomparing maps from different epochs is somewhat challenging given the resolution limit and varying types of data. Keep in mind that the maximum entropy map has its highest spatial resolution for the hemisphere centered at zero degree longitude. In fact, the resolution in this region is the highest of any map created to date and is controlled by the information contained in the mutual event light curves. The opposite hemisphere has the lowest resolution shown since this is constrained by rotational light curves from 1954 to 1986. Recall that the maximum entropy maps also had to assume that the surface was not changing over this time frame. We still do not know conclusively if this assumption is correct or not but we now have additional information from Schaefer et al. (2008) that claims the light curve mean decreased by 5% between 1933 and 1954. Nonetheless, it appears that present-day surface is undergoing change at a level that is precluded by the data from the 1954 to 1989 time frame.

Throughout this entire time span of data (1933 to present day) the sub-solar point has moved from nearly pole-on in the southern hemisphere (bottom of map) to now being ever more pole-on in the north. There is also a strong correlation in viewing geometry over this time as well. The MaxEnt map had the polar units at their maximum foreshortening while still being able to see both regions. As our viewpoint moves ever northward that pole becomes less foreshortened and thus easier to measure. A striking result is that these maps indicate that the north polar regions are brighter now than in the past. It is possible that this result is more a consequence of an initially poorer determination of the polar albedo and not due to an actual change on the surface. If change were taking place at an observable level one might expect the north polar regions to be darkening instead as they get ever more insolation. However, we cannot rule out surface texture evolution that could brighten the surface (e.g., Grundy & Stansberry 2000; Eluszkiewicz et al. 2007).

Despite the differences in the maps, there are clearly features common to all. All maps show a dark province ranging from 80° to 160° longitude and +20° to –30° latitude. This is the region that is responsible for the deep minimum in the light curve. Likewise, the longitudes from 160° to 240° are generally bright and this is what gives rise to the light curve maximum. The brightest region noted in the past work was at (0, 180) that has been reported by Grundy & Buie (2001) to be rich in CO ice. This location continues to be the brightest point in the new map and appears to be more neutral in color from both the FOC and ACS data. This region is included in the close-approach hemisphere for the New Horizons encounter—chosen for its range of albedos and spectral diversity.

The maps of Charon shown present a very different story. First, the resolution of *HST* is not really high enough to return very much spatial resolution on the surface of Charon. In reality, most of the constraint is longitudinal as informed by the light curve. The old maximum entropy map for Charon from Buie et al. (1997) looks very different from this new map. However, Buie et al. (1997) warned that the Charon map was not likely to be very accurate—a prediction that seems now to be confirmed. The MaxEnt mapping process did not have enough data constraints to truly solve for a global map and the

consequence was to mix a copy of Pluto’s map in with any signal that might have come from Charon on the anti-Pluto hemisphere. Clearly, the strong longitudinal modulation in the MaxEnt map is spurious. However, the resolved albedo information on the sub-Pluto hemisphere that was constrained by the mutual event data may yet prove to be useful.

The one notable feature in the Charon maps is the general latitudinal trend of albedo. Both filters show a general brightening near the equator and drop in albedo toward the poles. These data also seem to indicate that the south polar region is somewhat darker than the north but the significance of this finding is hard to pin down. Numerous tests were made during the fitting process to determine if this was a stable answer. One can imagine that such a latitude trend might be correlated with position fitted for Charon. We restarted the fitting process by forcing slightly different positions, systematic changes to focus, and returning the map to a uniform mean albedo. In all cases, the converged map returned to the version shown giving us some confidence that the result is at least consistent with the images. In addition, we have astrometric data that has been independently analyzed (Tholen et al. 2008) for Charon and there is no meaningful difference in the positions fitted based on a fixed, uniform map versus the fitting that involved the map as a free parameter.

Continued observations by *HST* that return both light curve and maps will be essential for constraining the evolution of the surface. The current low-galactic latitude for Pluto makes light curve work difficult but fortunately *HST* data do not suffer this complication. Also, we have seen a more complex light curve behavior emerge with ever lower phase angles and make it much more important to get accurate resolved photometry. While low galactic latitude makes ground-based work more difficult it also dramatically increases the opportunities for stellar occultations that can directly constrain the atmospheric and geometric properties. The combination of continued occultation and *HST* observations will provide some of the best constraints on seasonal evolution of the surface and atmosphere.

## 7. CONCLUSION

We present disk-resolved *HST* ACS imaging of Pluto and Charon obtained during 2002–2003. These data are used to construct two-color albedo maps of Pluto and Charon. The similar inversion techniques are also applied to earlier 1994 FOC images to obtain comparable Pluto maps from that epoch. These maps, along with a previous generation of maps from inversion of mutual event and light curve data, are consistent with an emerging picture of Pluto’s surface as the visible face of a complex and dynamically interacting surface–atmosphere system.

While several gross albedo features persist over the three epochs of maps considered, some of the details are clearly changing in ways that cannot simply be explained by the slowly changing aspect of Pluto’s surface as seen from the inner solar system. Indeed, observable changes at blue wavelengths occur over the single-year interval between the 2002 and 2003 observations. The general trends of brightening of the northern pole which is subject to increasing insolation and darkening of lower latitude regions which are receiving less sunlight may be contrary to expectation for seasonal removal of bright volatile ices from areas receiving the most sunlight accompanied by condensation in areas receiving less. But similar expectations were shown to be faulty when *Voyager II* imaged Triton, revealing the southern polar cap to be bright compared with darker equatorial regions, despite receiving continual sunlight

which should be driving net sublimation of nitrogen ice, coupled with condensation in lower latitude regions. While several ideas have been proposed to account for the unexpected albedo patterns on Triton, the seasonal behavior of volatile ices on both bodies remains poorly understood. Ongoing observations are needed to monitor the continuing seasonal trends and, for Pluto, to provide context for New Horizons' brief, but in-depth exploration of the system in 2015.

Our new albedo maps have a variety of uses. The maps can be used to improve volatile transfer models by providing improved constraints on the heat input into the system. These results also permit an exploration of the diversity of coloration of Pluto's regions, as well as rendering how their colors might appear to the human eye. We can now compute the effect of Pluto's variegated surface on its apparent astrometric location when its disk is unresolved. Since Pluto and Charon are tidally locked, albedo patterns which shift the observed COL can become entangled with orbital parameters which shift the relative locations of Pluto and Charon. Since the attempted repair of ACS/HRC was not successful, these map products are most likely the only optical maps we will see of Pluto prior to the New Horizons encounter. Other, lower spatial resolution, observations will continue but these maps will provide a critical baseline from which to continue studying the Pluto system.

This paper is based on observations with the NASA/ESA *HST* obtained at the Space Telescope Science Institute, which is operated by the Association of Universities for Research in Astronomy, Incorporated, under NASA contract NAS5-26555. Support for this work was provided by NASA through grant numbers *HST*-GO-09391.01-A, *HST*-GO-10786.01, and *HST*-AR-10940.01 from STScI. Special thanks to Andy Lubenow (1956–2005) at STScI for his exemplary support of this project.

## APPENDIX

### SUPPLEMENTARY MATERIALS

#### A.1. Map files

During the modeling process, the maps are encoded as a series of free parameters that are linked to areas on the surfaces. The supplemental file `srcfiles.tar.gz` available in the online journal contains the files that describe the underlying model. Also included is some sample IDL code that illustrates how to read these files and generate a map.

The supplemental file `fig05.tar.gz` available in the online journal contains maps of Pluto as shown in Figure 5 plus all of the other versions of the maps based on the different photometric parameter sets described in Table 2. These maps are provided both as single-scattering albedo maps and as  $I/F$  maps computed at an incidence angle of  $0^\circ$  and an emission angle of  $1^\circ$  (thus  $1^\circ$  phase angle). The supplemental file `file07.tar.gz` available in the online journal contains the same type of information for Charon as shown in Figure 7.

The file `fig11.tif` available in the online journal is a color image that contains the information displayed in 12 except that  $0^\circ$  longitude is at the left side of the image. This information is proportional to normal albedo but is not really intended as a product to support photometric investigations.

The file `fig12.tif` available in the online journal is a false-color image that contains the information displayed in 11 except that  $0^\circ$  longitude is at the left side of the image.

#### A.2. Tabular Data

The calculations in this work require numerous geometric and ancillary quantities to fully describe the observations and the control parameters of the model. The file `supptab.fits` is a FITS-format ASCII table with 35 columns of data used by the modeling software to extract the Pluto maps from the ACS/HRC data. The header of the file contains a description of each column in the table. These quantities include such values as exposure time, filters used, sub-Earth latitude and longitude, source position on the image, and more. Each row in the table gives the information for each image, 384 images in all.

## REFERENCES

- A'Hearn, M. F., Ohlmacher, J. T., & Schleicher, D. G. 1983, TR AP83-044 (College Park, MD: Univ. Maryland)
- Anderson, J., & King, I. R. 2004, STScI ISR ACS 2004-15
- Brown, M. E., & Trujillo, C. A. 2004, *AJ*, **127**, 2413
- Buie, M. W., Grundy, W. M., Young, E. F., Young, L. A., & Stern, S. A. 2006, *AJ*, **132**, 290
- Buie, M. W., & Tholen, D. J. 1989, *Icarus*, **79**, 23
- Buie, M. W., Tholen, D. J., & Horne, K. 1992, *Icarus*, **97**, 211
- Buie, M. W., Tholen, D. J., & Wasserman, L. H. 1997, *Icarus*, **125**, 233
- Colina, L., Bohlin, R. C., & Castelli, F. 1996, *AJ*, **112**, 307
- Eluszkiewicz, J., Cady-Pereira, K., Brown, M. E., & Stansberry, J. A. 2007, *J. Geophys. Res.*, **112**, E06003
- Grundy, W. M., & Buie, M. W. 2001, *Icarus*, **153**, 248
- Grundy, W. M., & Stansberry, J. A. 2000, *Icarus*, **148**, 340
- Hapke, B. 1981, *J. Geophys. Res.*, **86**, 3039
- Hapke, B. 1984, *Icarus*, **59**, 41
- Hapke, B. 1993, *Combined Theory of Reflectance and Emittance Spectroscopy* (New York: Cambridge Univ. Press)
- Khare, B. N., Sagan, C., Heinrich, M., Thompson, W. R., Arakawa, E. T., Tuminello, P. S., & Clark, M. 1994, *BAAS*, **26**, 1176
- Krist, J. 2004, <http://www.stsci.edu/software/tinytim/tinytim.html>
- Marcialis, R. L. 1988, *AJ*, **95**, 941
- Mustard, J. F., & Bell, J. F., III. 1994, *Geophys. Res. Lett.*, **21**, 353
- Schaefer, B. E., Buie, M. W., & Smith, L. T. 2008, *Icarus*, **197**, 590
- Sicardy, B., et al. 2006, *Nature*, **439**, 52
- Sirianni, M., et al. 2005, *PASP*, **117**, 1049
- Spencer, J. R., Calvin, W. M., & Person, M. J. 1995, *J. Geophys. Res.*, **100**, 19049
- Stern, S. A. 1992, *ARA&A*, **30**, 185
- Stern, S. A., Buie, M. W., & Trafton, L. M. 1997, *AJ*, **113**, 827
- Tholen, D. J., & Buie, M. W. 1997, *Icarus*, **125**, 245
- Tholen, D. J., Buie, M. W., Grundy, W. M., & Elliot, G. T. 2008, *AJ*, **135**, 777
- Wagner, J. K., Hapke, B. W., & Wells, E. 1987, *Icarus*, **69**, 14
- Young, A. T. 1984, *Icarus*, **58**, 197
- Young, L. A., et al. 2008, *Space Sci. Rev.*, **140**, 93